Force-generating apoptotic cells orchestrate avian neural tube bending

Daniela Roellig, Sophie Theis, Amsha Proag, Guillaume Allio, Bertrand Bénazéraf, Jérôme Gros, Magali Suzanne

Short Article

Developmental Cell

Force-generating apoptotic cells orchestrate avian neural tube bending

Graphical abstract

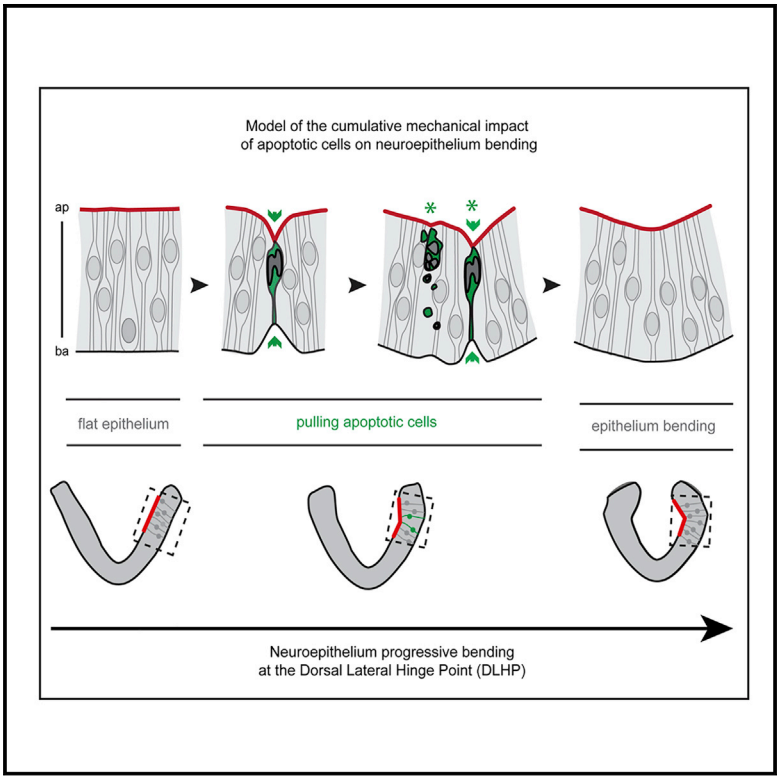

Authors

Daniela Roellig, Sophie Theis, Amsha Proag, Guillaume Allio, Bertrand Bénazéraf, Jérôme Gros, Magali Suzanne

Correspondence

magali.suzanne@univ-tlse3.fr

In brief

The vertebrate neural tube, the precursor of the nervous system, forms through successive bendings of the neuroepithelium at the midline and at the dorsal folds. Roellig et al. show that dying cells, which are more concentrated at the dorsal folds, exert repetitive pulling forces locally and thus contribute to the final shape of the neural tube.

Highlights

- Apoptotic cells are force-generating cells in the avian neural tube
- Apoptotic force drives the upward movement of the nucleus and nuclear fragmentation
- Apoptotic cells cumulatively impact the neighboring tissue
- Apoptotic force mechanical impact participates in progressive bending of the neural tube

Roellig et al., 2022, Developmental Cell *57*, 707–718
March 28, 2022
https://doi.org/10.1016/j.devcel.2022.02.020

CellPress

Developmental Cell

CellPress
OPEN ACCESS

Short Article

Force-generating apoptotic cells orchestrate avian neural tube bending

Daniela Roellig,[1] Sophie Theis,[1,2] Amsha Proag,[1] Guillaume Allio,[1] Bertrand Bénazéraf,[1] Jérôme Gros,[3] and Magali Suzanne[1,4,*]

[1]Centre de Biologie Intégrative, CNRS/UMR 5088, Université Toulouse III, Toulouse, France
[2]Morphogénie Logiciels, 32110 St Martin d'Armagnac, France
[3]Institut Pasteur, CNRS/UMR 3738, Paris, France
[4]Lead contact
*Correspondence: magali.suzanne@univ-tlse3.fr
https://doi.org/10.1016/j.devcel.2022.02.020

SUMMARY

Apoptosis plays an important role in morphogenesis, and the notion that apoptotic cells can impact their surroundings came to light recently. However, how this applies to vertebrate morphogenesis remains unknown. Here, we use the formation of the neural tube to determine how apoptosis contributes to morphogenesis in vertebrates. Neural tube closure defects have been reported when apoptosis is impaired in vertebrates, although the cellular mechanisms involved are unknown. Using avian embryos, we found that apoptotic cells generate an apico-basal force before being extruded from the neuro-epithelium. This force, which relies on a contractile actomyosin cable that extends along the apico-basal axis of the cell, drives nuclear fragmentation and influences the neighboring tissue. Together with the morphological defects observed when apoptosis is prevented, these data strongly suggest that the neuroepithelium keeps track of the mechanical impact of apoptotic cells and that the apoptotic forces, cumulatively, contribute actively to neural tube bending.

INTRODUCTION

The folding of an epithelium is a basic morphogenetic procedure where a two-dimensional sheet is transformed into a three-dimensional structure (Davidson, 2012; Pearl et al., 2017). This process is crucial to shape organs during the embryonic development. Apical constriction plays a key role in tissue remodeling, particularly in tissue invagination (Martin and Goldstein, 2014). Molecular motor nonmuscle myosin II, in association with filamentous actin (Lecuit et al., 2011), generates forces either at the level of adherens junctions, forming a cortical ring (Chanet and Martin, 2014; Heisenberg and Bellaïche, 2013; Umetsu and Kuranaga, 2017), or in an sub-apical domain, forming a medio-apical meshwork (Martin et al., 2009). In addition to apical constriction, recent studies in different invertebrate species identified a mechanism of tissue invagination where orthogonal forces cause apico-basal cell shortening (Gracia et al., 2019; Monier et al., 2015; Sherrard et al., 2010; Sui et al., 2018; Sui and Dahmann, 2020; Yang et al., 2017).

The formation of the neural tube, which gives rise to the central and peripheral nervous systems, has served as a paradigm of vertebrate embryonic morphogenesis for decades. Bending of the initially flat neural epithelium begins with the local apical constriction of cells along the embryonic midline called the median hinge point (MHP). Next, the bilateral bending of the dorsal part of the neural plate at the so-called dorsolateral hinge points (DLHPs) opposes the two neural folds that eventually fuse and enclose a hollow tube (reviewed in the study conducted by Nikolopoulou et al., 2017). During this bending, the initially convex neural plate progressively adopts a concave shape (Morriss-Kay, 1981). Notably, failure in any step of this morphological process perturbs the neural tube closure and causes neural tube defects, which are among the most common birth defects (Copp and Greene, 2010; Mitchell, 2005).

Bending at the MHP relies on several cellular mechanisms such as apical constriction driven by planar-polarized actomyosin (Nishimura et al., 2012; Nishimura and Takeichi, 2008; Sullivan-Brown and Goldstein, 2012) and the acquisition of wedge-shaped midline cells triggered by basally located nuclei (Schoenwolf, 1985; Smith and Schoenwolf, 1989; Smith et al., 1994). Bending at DLHP is also important for the proper closure of the trunk neural tube (Elms et al., 2003; Ybot-Gonzalez et al., 2007); however, the cellular mechanisms involved are poorly understood (McShane et al., 2015; Schoenwolf and Franks, 1984; Smith and Schoenwolf, 1988).

Apoptosis (programed cell death) is highly present during neural tube formation (Gibson et al., 2011; Hirata and Hall, 2000; Honarpour et al., 2001; Massa et al., 2009; Weil et al., 1997; Yamaguchi et al., 2011). Interestingly, the impairment of apoptosis inhibits or delays the neural tube closure both in chicken and in mice (Cecconi et al., 1998; Hakem et al., 1998; Houde et al., 2004; Kuida et al., 1998; Kuida et al., 1996; Massa et al., 2009; Urase et al., 2003; Weil et al., 1997; Yamaguchi et al., 2011; Yoshida et al., 1998). However, although these data reveal an

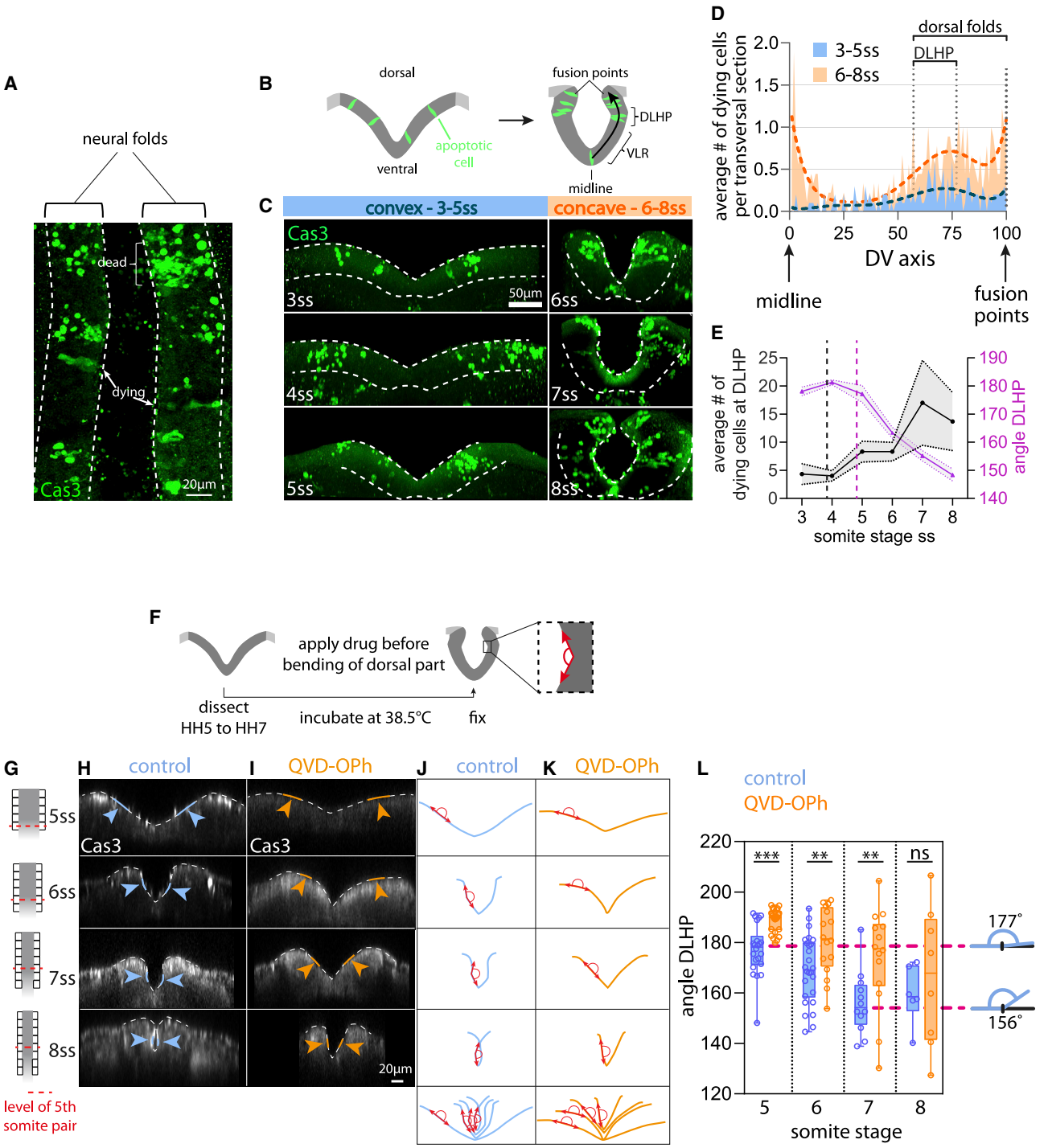

Figure 1. Apoptosis is highly present at the DLHP and is required for the bending of DLHP (see also Figure S1)

(A) Cas3 staining in the trunk region of whole-mount embryo (HH9) indicating cells in the process of dying (arrows) and dead cells (bracket). Dotted lines outline the neural folds.

(B) Schematics of neuroepithelium before (left) and after (right) bending at DLHP. Apoptotic cells (green) along DV axis (black arrow) were quantified between the ventral midline and dorsal fusion points of the neuroepithelium (dark gray). VLR = ventrolateral region.

(C) 100-µm depth projections of transversal sections of Cas3 immunostained embryos at 3–8 ss.

(D) Distribution of average number of dying cells per transversal section along DV axis.

(E) Quantification of dying cells (black) and the angle measured at the DLHP (purple) over time.

(F) Schematics of experimental design for QVD-OPh drug treatment.

(legend continued on next page)

intriguing link between apoptosis and morphogenesis in vertebrates, the molecular, cellular, and biophysical mechanisms remain unknown.

During apoptosis, cell morphology changes dramatically with cell shrinkage, membrane blebbing, and, most of the time, fragmentation of the cell into apoptotic bodies (Häcker, 2000; Kerr et al., 1972). It has long been acknowledged that apoptosis partakes in tissue remodeling (for reviews, see the studies conducted by Hernandez-Matinez and Covarrubias, 2011 and Fuchs and Steller, 2011). However, its impact has been mainly considered as a consequence of local cell elimination instead of an active involvement of apoptotic cells in tissue remodeling. It is only recently that a nonautonomous impact of apoptotic cells on their surroundings has been discovered, and the cellular mechanisms are only starting to be understood (Monier et al., 2015; Pérez-Garijo et al., 2013; Suzanne et al., 2010; Toyama et al., 2008).

Here, we use neural tube bending in avian embryos as a model to explore the dynamics of apoptotic cells and decipher how they impact the surrounding tissue. We found that apoptosis occurs at a high frequency at the DLHP of the neural tube shortly before or at the time of bending and revealed that apoptosis plays a role in DLHP morphogenesis. We show that an actomyosin cable spreads along the apico-basal axis of the dying cell and generates an apico-basal force before cell extrusion. The contraction of this cable coincides with a fast apico-basal displacement of the apoptotic nucleus dependent on myosin II contractility and with apical and basal deformations. These deformations were partly maintained, leading us to propose that apoptotic neighbors keep some memory of the apoptotic force. This transient force would lead to a progressive deformation of the epithelium and thus participate in epithelium bending.

RESULTS

Apoptosis is highly increased at DLHP and required for neural tube bending

As a first step to define how apoptosis participates in neural tube morphogenesis, we mapped the spatiotemporal occurrences of apoptotic cells during neural plate folding (Figure S1A, orange and blue arrowheads; Video S1) and neural tube closure (Figure S1A, red arrowhead) of chicken embryos, focusing particularly on trunk neural tissue (Figure S1B) where apoptosis is highly abundant (Figures 1A and S1C and S1E). We found that apoptotic cells tend to appear in the trunk neural plate at the 3-somite stage and persist until the complete closure of the tube. Interestingly, the zone with high apoptotic density extends progressively to the posterior region following somite formation (see rectangles in Figures S1C and S1D). We next quantified the distribution of apoptotic cells along the dorsoventral (DV) axis of the neural ectoderm. To precisely map the apoptotic pattern, we counted only cells that were in the process of dying (STAR Methods) rather than the post-apoptotic fragments of cells, which tend to relocate within the epithelium. From 3 ss to 5 ss, apoptosis was low and randomly distributed along the DV axis of the neural tube, with a frequency slightly higher in the most dorsal part (commonly called dorsal folds), particularly in the region of the future DLHP (Figures 1C and 1D). At later stages (from 6 ss to 8 ss), the level of apoptosis increased and a preferential accumulation of apoptotic cells was visible both at the midline, which had already bent (Figures 1C and 1D), and in the DLHP region and more generally in the whole dorsal folds region, which interestingly changed its shape from convex to concave at around 6 ss (Figure 1C). As a consequence, we chose to focus on dorsal folds morphogenesis. We further plotted the number of apoptotic cells together with the angle of the apical surface in the DLHP region over time. We found that the increase of apoptosis slightly precedes tissue bending at the DLHP, highlighting a tight spatial and temporal correlation between apoptosis and the neural plate bending at the DLHP region in the avian neural tube (Figure 1E).

This led us to hypothesize that apoptosis might influence neural tube morphogenesis by taking part in the bending of the neural epithelium at the DLHP. In order to test this hypothesis, we inhibited apoptosis prior to the dorsal bending of the neural epithelium. We treated the embryos with the broad-spectrum caspase inhibitor QVD-Oph (summarized in Figure 1F, see STAR Methods), which drastically reduces the number of apoptotic cells in the neural tube (Figures S1F and S1G). We then measured the angle of the neural epithelium at the level of the predicted or present DLHP at the position of the 5th somite pair (STAR Methods), which constitutes the central region of the apoptotic domain. We found that the QVD-OPh treatment significantly impeded bending at the DLHP in 5–7 ss embryos and showed the same tendency in 8 ss embryos (Figures 1G–1L). On the contrary, the bending at MHP is mostly unaffected in these conditions (Figure S1H), which is consistent with the fact that apoptosis appears in this region when MHP bending is already well advanced (Figure 1C). These data identify the bending at the DLHP as a specific aspect of neural tube remodeling relying on apoptosis.

Apoptotic cells generate forces during avian neural tube formation

To decipher how apoptotic cells, which are going to be eliminated and will not be part of the final organ, can influence neural epithelium bending, we investigated the dynamics of apoptotic cells focusing on the dorsal part of the neuroepithelium (Figure 2A).

Interestingly, we frequently noticed a strong deformation of the apical surface around the apoptotic cells that had adopted a bottle shape, whereas cell-cell adhesions were maintained and the apical surface was reduced (Figure 2B, blue arrow).

(G) Schematics showing the 5th somite pair at different developmental stages. Gray = neural epithelium, black rectangles = somites, and red dotted line = level of section.

(H and I) Transversal sections at the level of the 5th somite pair of control (H) or QVD-OPh-treated (I) embryos at the 5–8 somite stage and Cas3 staining. Arrowheads and blue/orange lines indicate the site of angle measurement.

(J and K) Outline of apical curvature (blue/orange lines) of the neuroepithelium of control (J) or QVD-OPh-treated (K) embryos shown in (H) and (I). Red arrows indicate angle at DLHP.

(L) Boxplot quantification of angle measured at the (predicted) DLHP at the level of the 5th somite pair in embryos at 5–8 somite stage.

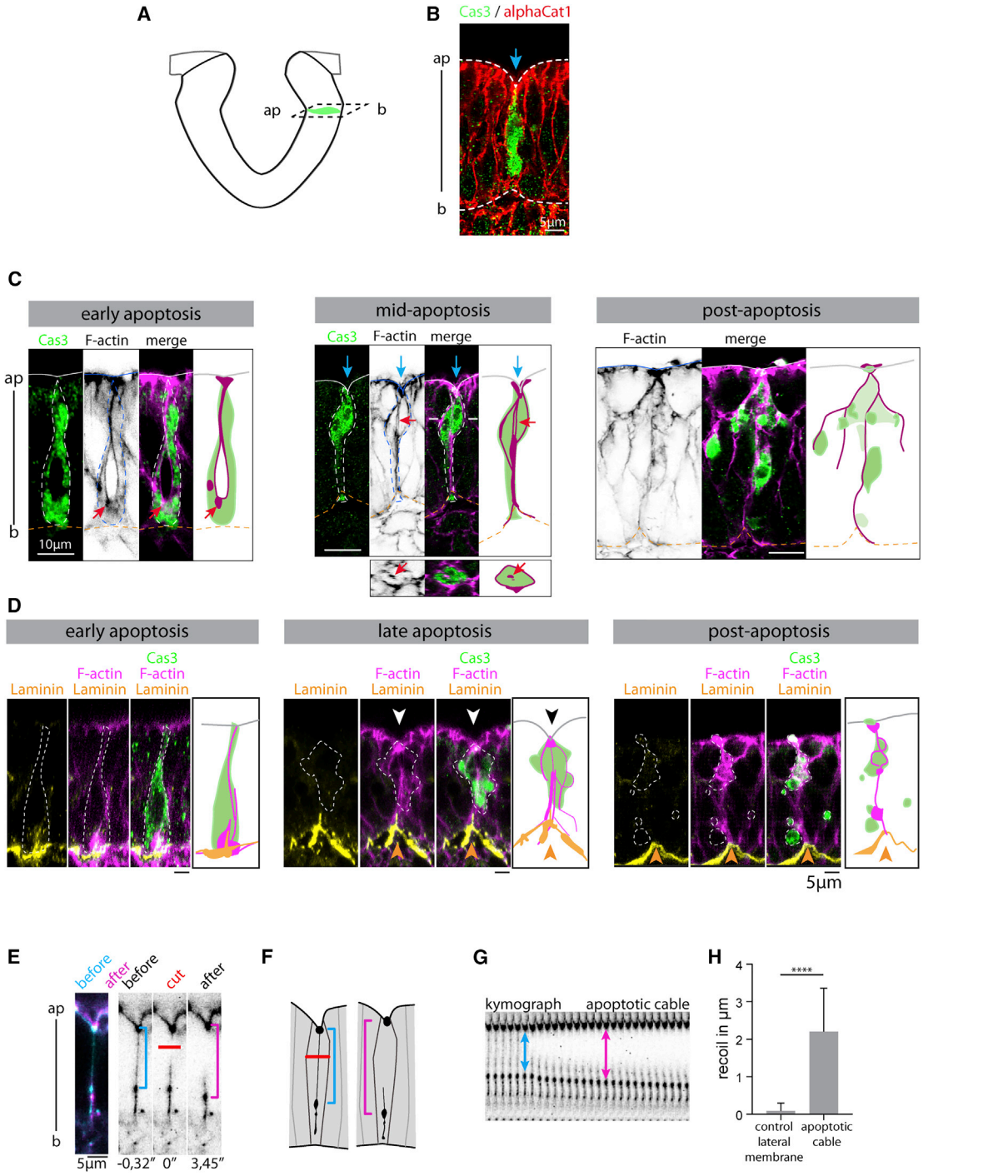

Figure 2. Apoptotic cells are force-generating cells in the neural tube (see also Figure S2)

(A) Position of sections shown in (B–E). Ap = apical, b = basal.

(B) Cas3 (green) and alpha-catenin 1 (red) stainings. Basal and apical sides are outlined in (B) and (C).

(C and D) Stainings of apoptotic cells (outlined with white dotted lines) at early (left), mid-(middle) and post-(right) apoptotic stages and schematics with Cas3 (green) and Phalloidin (magenta) in (C) and (D) and Laminin (yellow) in (D). (C) Apical deformation (blue arrow). Actin cables (red arrow). Lower middle panel: section through apoptotic cell at the level of white lines in upper panel. Cable in the middle of the cell mass (red arrow). (D) Apical and basal deformations (arrowheads). Note that apical deformation is observed in 91% of mid- and late apoptotic cells (n = 21/23 cells from 13 embryos). Basal deformation was observed in 88.8% of mid- and late apoptotic cells (n = 8/9 from 4 embryos).

(legend continued on next page)

This suggests the presence of either a pushing force from its neighbors or a pulling force from the apoptotic cell. To further investigate which cells are generating the force responsible for this deformation, we characterized actomyosin cytoskeleton dynamics during the apoptotic process by time-lapse confocal imaging. To visualize the dying cells in living tissues in avians, we adapted the apoptosensor GC3Ai (Schott et al., 2017; Zhang et al., 2013), a modified GFP that becomes fluorescent after cleavage by the effector caspases (STAR Methods). Similar to what has been described in *Drosophila* tissues (Schott et al., 2017), this construct served to detect apoptosis just before or at the time of apical constriction in avian embryos. We then co-electroporated the apoptosensor with either an actin marker or a marker of nonmuscular myosin II (Figures S2A and S2B) and followed the cytoskeletal dynamics. We observed that apoptotic cells, after adopting a bottle shape with actin accumulations basally (orange arrowhead), formed an apico-basal actomyosin cable that traversed the cell mass (Figures S2A and S2B, blue and red brackets). This cable shortened, which coincided with an apico-basal shortening of the dying cell (orange brackets), suggesting an apico-basal contraction of the cable. Then, the cell fragmented.

We further characterized the impact of actomyosin cable contraction in fixed samples. In the bottle-shaped cells, the actin cortex was strongly increased all around the cell and the apical and basal surfaces of the epithelium were mostly flat (Figures 2C and 2D, early apoptosis). In the cells that were more advanced in the apoptotic process, according to a similar cell shape as in live imaging (Figures S2A and S2B), we observed an apical deformation that coincided with actin cables that intersected the cell mass from apical to basal (Figure 2C, mid-apoptosis, blue and red arrows, respectively). A similar deformation was observed on the basal part of the dying cell when the cell contracted as illustrated by the deformation of the basal membrane (Figure 2D, late apoptosis), although the basal surface of the neuroepithelium is globally more irregular than the apical surface (Figures S2C and S2D). Then, the cell fragmented, which concurred with the formation of apoptotic bodies (Figures 2C and 2D, post-apoptosis). Finally, both apical and basal deformations were synchronously observed by live imaging following the dynamics of single apoptotic cells (Figure S2E).

Thus, apoptotic cells in the vertebrate neuroepithelium form an apico-basal actomyosin cable that extends all along the apico-basal axis of the cell and contracts while a local and transient deformation on the apical and basal side of the epithelium is observed (Figures 2C, 2D, and S2E). Therefore, we hypothesized that the actomyosin cable is indeed exerting a force in the apico-basal plane of the apoptotic cell.

To test this hypothesis, we turned to laser ablation. We targeted cables that spanned the epithelium apico-basally in cells with a clear apical or basal deformation and are specifically present in apoptotic cells (Figures S2I and S2J). We observed a recoil significantly higher than the one observed in control areas (Figures 2E–2H and S2F–S2H; Video S2). These results showed that the actomyosin cable in the neuroepithelium is indeed under tension while the rest of the epithelium bears very low apico-basal tension, demonstrating that the apoptotic cells in the neural tube are force-generating cells capable of deforming both the apical and the basal surfaces of the epithelium.

Tight connection between the apoptotic nucleus and the actomyosin cable

We then asked what the cellular mechanism responsible for the generation of this pulling force was. We found that the actomyosin cable contacts the apoptotic nucleus and decided to characterize this interaction. In early apoptotic cells, actin accumulated below the nucleus (Figures 3A and 3A′, red arrowhead) before any clear sign of an actomyosin cable, while the nucleus had an oval shape (Figure 3A), similar to nonapoptotic neuroepithelial nuclei (Figure S3B). In cells where an apico-basal actin cable had formed, apoptotic nuclei appeared deformed (Figures 3B and 3C, yellow arrowheads), while a strong actin accumulation was observed just below the nucleus (red arrowhead). Double immunostainings for actin and phospho-myosin II further revealed an accumulation of these two cytoskeletal markers below the nucleus, forming a basket-like structure around the nucleus (Figure S3C).

Thus, the nucleus seemed tightly linked to the actomyosin. Indeed, in transversal sections, we could visualize the actin cable in the middle of the nuclear mass, suggesting that either the cable traverses the nucleus or the nucleus is wrapped around the actin cable (Figures 3B′ and 3C′, blue arrowheads). To discern between these two options, we used immunodetection of Lamin, a protein of the inner nuclear membrane. In apoptotic cells that were still attached apico-basally and had an unfragmented nucleus, we observed the presence of Lamin within the nuclear region where the actin cable was present, suggesting that the nucleus is wrapped around the cable, forming a tight connection between the nuclear envelope and the cable (Figure 3D).

We then looked at myosin activity by time-lapse imaging. We observed that while myosin formed a linear structure all along the apico-basal axis of the dying cells, stronger accumulations of myosin coincided spatially and temporally with the basal and apical deformations of the nucleus (Figures 3E, E', E'', white/blue arrowheads and arrows; Video S3) , suggesting a direct impact of myosin contraction on nucleus shape. The nuclear deformation also coincided with the apical pulling (Figures 3B and 3C), suggesting that both depend on the contraction of the actomyosin cable. Interestingly, in parallel to these deformations, the apoptotic nucleus underwent an upward movement from basal to apical. Finally, the nucleus deformed further and started to fragment (Figure 3E‴, arrowheads). Altogether, these data suggest that the nucleus is pulled upward, deformed, and fragmented by the actomyosin network.

(E–H) Laser ablation of apico-basal myosin cable in transgenic quail embryos with cytoskeleton markers. Brackets and arrows indicate the actin cable before (cyan) and after (magenta) laser ablation in images extracted from movie (E), in schematics (F) and kymograph (G). Red line = ablation site.
(H) Quantification of recoil. Please note that the acquisition has been done in a single z section, focusing either on basal or on apical anchoring point, preventing any comparison between apical and basal release.

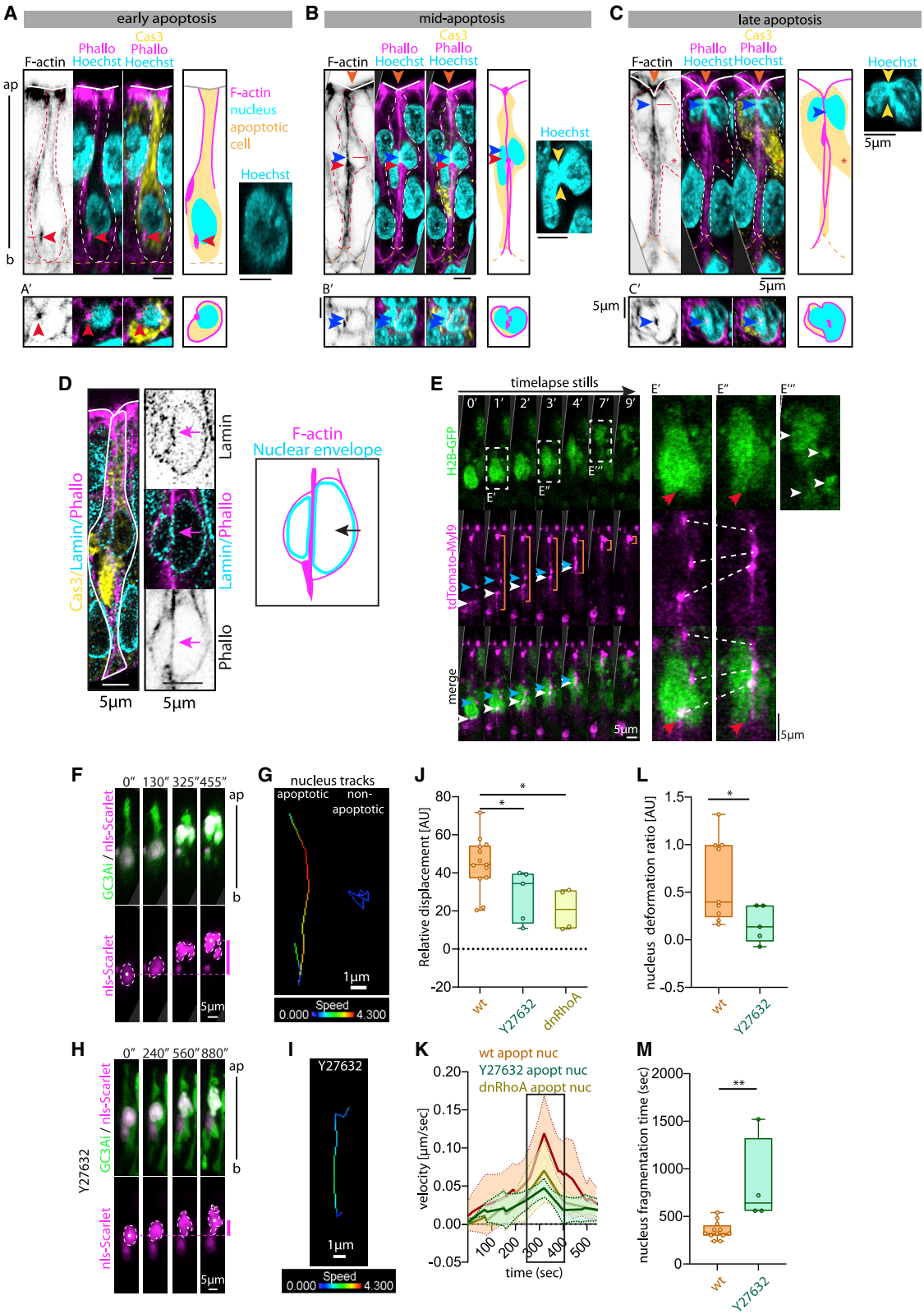

Figure 3. Apoptotic nucleus dynamics in neuroepithelial cells (see also Figure S3)

(A–C) Sagittal sections and corresponding schematics of neuroepithelial apoptotic cells. (A′–C′) Transverse sections at the level of the red lines in A–C are shown in A′–C′ and magnification of nucleus on right side. Cas3 = yellow, Phalloidin = gray or magenta, and Hoechst = cyan. White/red dotted lines = outline of apoptotic

(legend continued on next page)

The apoptotic force participates to nucleus dynamics and fragmentation

To characterize nuclear dynamics during the apoptotic process, we next tracked and quantified the position, the displacement, and the velocity of apoptotic nuclei (Figure 3F; Video S4), compared with nonapoptotic nuclei (Figures S3D–S3F). As expected, nonapoptotic nuclei were found along the whole length of the apico-basal axis (Figure S3D, blue boxplots), which is characteristic of pseudo-stratified epithelia (Figure S3B). In apoptotic cells, however, as described above, the nucleus, which was initially situated at the basal side of the neural epithelium, moved upwards (Figures S3D and S3E, orange boxplots) and reached the apical side when the cell started fragmenting (Figure 3F, last panel), which marks the end of apoptosis. Furthermore, while nonapoptotic nuclei were mostly immobile at the time scale of our analysis, apoptotic nuclei showed a velocity peak just before the nucleus reached the apical side (Figures 3G and S3F).

To characterize the role of myosin in apoptotic nucleus dynamics, we next inactivated myosin II, either by using the Rock inhibitor Y27632 (Uehata et al., 1997), which has been described as preventing neural tube closure (Kinoshita et al., 2008; Wei et al., 2001), or by expressing a dominant-negative form of Rho (Nakaya et al., 2008). We imaged and tracked the nucleus movement of apoptotic cells in these two conditions (Figures 3H and 3I; data not shown). Interestingly, we noticed that both the distance traveled by these apoptotic nuclei and their velocity were strongly reduced (Figures 3J and 3K), indicating that the apoptotic nucleus is indeed pulled up by the actomyosin cable. We further quantified the nuclear deformation and found that nuclei were less deformed than in the wildtype context (Figure 3L) and that fragmentation is delayed (Figure 3M).

Altogether, these data indicate that nuclei upward movement and deformation depend on actomyosin cable contraction, which appears necessary for proper nucleus fragmentation. They further suggest that the apoptotic nuclei could create a resistance necessary to deform both the apical and basal surfaces of the epithelium.

Impact of apoptotic cell on the surrounding tissue

We next asked how the transient deformation generated at the level of individual dying cells might lead to a large-scale reorganization of the surrounding tissue and contribute to the neural tube bending in the DLHP region, where apoptotic cells are abundant. We wondered whether the deformation induced by apoptotic cells was reversible or persisted partially, somehow memorizing the mechanical impact of the individual apoptotic forces. To test this hypothesis, we further characterized and quantified the dynamics of apical surface deformation during and after apoptotic cell contraction and fragmentation. We measured the displacement of the apical surface of the epithelium at the level of a single apoptotic cell over time (Figure 4A) and determined the angle of the apical surface (Figure 4B), the speed of the deformation during contraction and release (Figure 4C), and the duration of the different steps (Figure 4D). Interestingly these data indicate that while the contraction takes about 10′, the release after apoptotic cell fragmentation is not instantaneous. This delay in apical release, already observed before DLHP bending (early stage, 1–3 ss), is getting stronger just before and when the epithelium starts to bend (4–6 ss). This indicates that apical deformations persist long after apoptotic cells fragment and that this persistence increases at the time of tissue bending (Figure 4A). Given the high number of apoptotic events, these observations suggest that apoptotic forces contribute to the final bending through a "ratchet-like" mechanism.

To further understand how transient forces lead to permanent neuroepithelium bending, we characterized cellular rearrangements and myosin II dynamics in the DLHP region, which limited the analysis to early stages, when the tissue is still mostly flat, for technical reasons. As observed in other tissues, apoptotic cell neighbors reoriented over time, forming a characteristic "rosette" pattern around the extruding cell. Indeed, while neighboring cells were randomly oriented before the apical constriction of apoptotic cells, similar to what is observed around "non-apoptotic" control cells, they became oriented radially around the apoptotic reduced apex (Figures 4E, 4F, S4B and S4C). Interestingly, this rosette pattern was maintained over time, even after the generation of the apico-basal pulling force (see cross-section in Figure S4C), suggesting that these cells retain some topological memory of the apoptotic force exerted, which, cumulatively, impacts tissue dynamics globally.

We further analyzed the myosin II distribution in the trunk region of the neural tube, focusing on the apical surface of the epithelium, where the highest concentration of myosin II is observed. We first used live imaging to follow myosin II dynamics. In this set of experiments, while supracellular tensile cables could be observed in the MHP region, as previously described (Nishimura et al., 2012), no clear supracellular reorganization was observed in the DLHP (Figure S4A). We next

cell. Orange dotted lines = outline of basal side. Solid white line = outline of apical side. Red arrowheads = actin accumulations. Blue arrowheads = actin cable. Red asterisk in (C) indicates a cell bleb.

(D) Cas3 (yellow), Lamin (cyan), and Phalloidin (magenta) staining in apoptotic cell (solid line), closeup of nucleus and schematic. Arrow indicates actin cable wrapped with Lamin.

(E) Stills from a movie of embryo electroporated with H2B-GFP/tdTomato-MLC9. Bracket = extent of myosin cable. Arrowheads = myosin dots. Dotted rectangle = closeup of nucleus in (E′, E″, E‴). (E′, E″) Basal deformation of nucleus (arrow) coinciding with converging dot-like myosin accumulations (dotted lines). (E‴) Closeup of nuclear fragments (arrowheads).

(F) Stills of movie of GC3Ai/nls-Scarlet electroporated embryo. Purple line denotes the distance traveled by the nucleus.

(G) Representative tracks of an apoptotic nucleus (left) and a nonapoptotic nucleus (right).

(H and I) Stills of time lapse of embryo electroporated with GC3Ai/nls-Scarlet and treated with Y27632 (H) and representative track (I).

(J and K) Box plot quantification of relative displacement of apoptotic nuclei treated with Y27632 or electroporated with dn-RhoA within the epithelium based on nuclei tracking in time-lapse movies compared with control apoptotic nuclei (J) and their velocity plots (K).

(L) Box plot quantification of nucleus deformation of control apoptotic nuclei and Y27632-treated apoptotic nuclei.

(M) Box plot quantification of the fragmentation time of control apoptotic nuclei or Y27632-treated apoptotic nuclei.

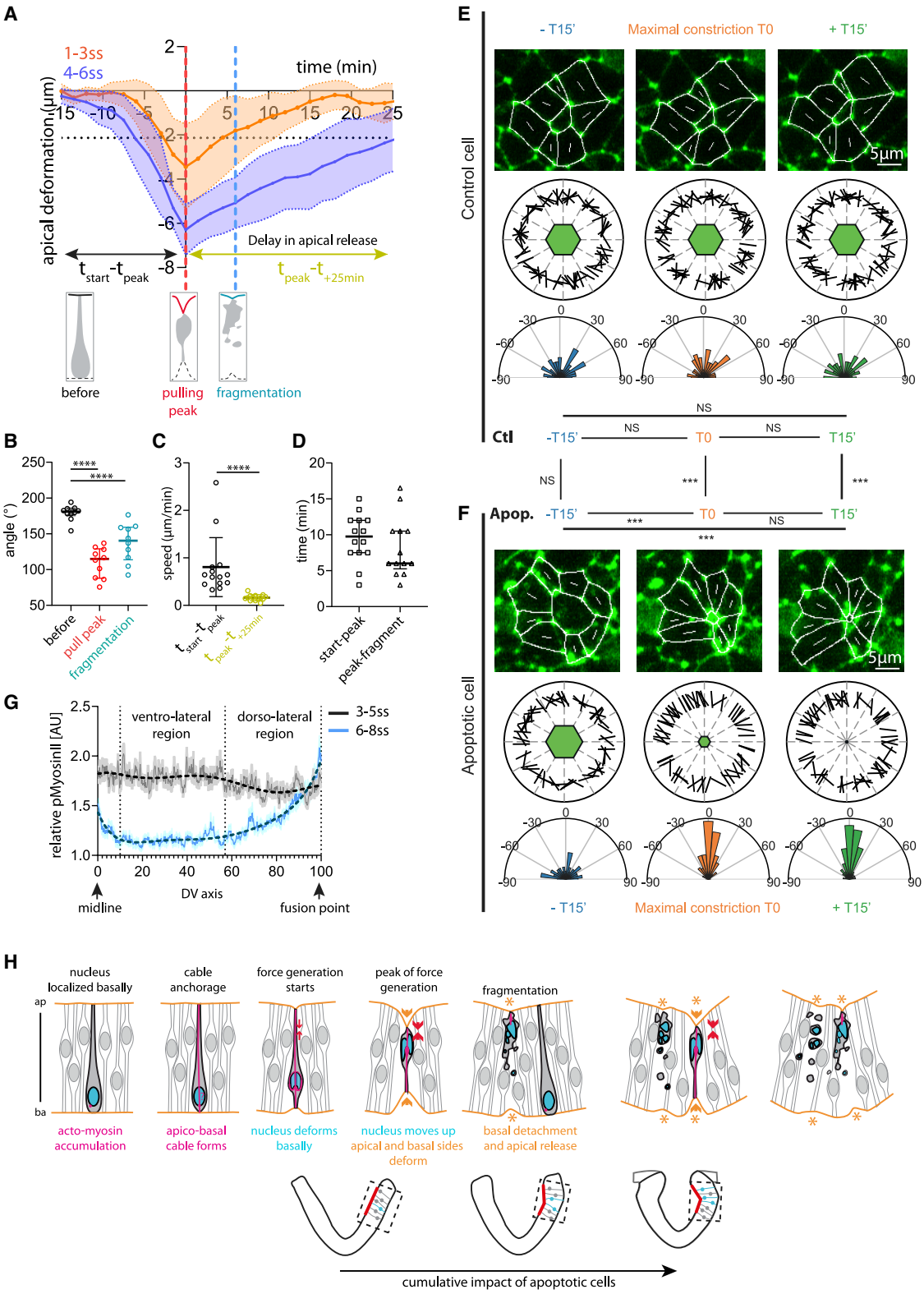

Figure 4. Apoptotic cells mechanically impact the neighboring tissue (see also Figure S4)

(A) Measurements of the apical deformation of cells undergoing apoptosis over time. Horizontal black dotted line: average level of apical side 25 min after pulling peak (−2.13 µm below initial level). Red dotted line: peak of apical pulling = t0. Blue dotted line: fragmentation time (average of 4–6 ss embryos). Schematics of

(legend continued on next page)

characterized the apical myosin II distribution along the DV on fixed samples. While myosin was homogeneously distributed along the DV axis of the neural tube at the early stage (3–5 ss), it is redistributed at the time of bending (6–8 ss) with a higher concentration in the dorsal region (including the DLHP) and at the midline (Figure 4G) and a relatively low level in the ventrolateral region (Figure S4A). This suggests that myosin II is stabilized and accumulates in the folding regions.

Altogether, our data show that apoptotic neuroepithelial cells create an apico-basal actomyosin-dependent force that is transmitted apically to the surroundings, progressively deforming the dorsal part of the neural tube and actively participating in its bending (Figure 4H).

DISCUSSION

Active role of apoptosis in vertebrates

Apoptosis is involved in a variety of morphogenetic processes; however, how cell elimination drives tissue remodeling is mostly unexplored in vertebrates. We used the morphogenesis of the neural tube as a model to study apoptosis-dependent morphogenesis in avian embryos. Our results show that apoptosis occurs preferentially at the DLHP, before and during the bending stage, and participates in DLHP bending through progressive deformation of the epithelium at the DLHP, revealing the origin of the failure in the neural tube closure previously observed. Thus, we reveal that far from being passively eliminated, apoptotic cells generate a force that constitutes a mechanical signal triggering tissue remodeling.

Conservation of the apoptotic force

Our results show that in avian embryos, apoptotic cells participate in tissue remodeling through the formation of apico-basal actomyosin cables that exert pulling forces on the apical surface. These observations are reminiscent of what has been observed recently in *Drosophila* (Monier et al., 2015). Altogether, these results reveal that the capacity of apoptotic cells to generate forces is an evolutionarily conserved mechanism.

Differences in the cellular mechanism

We observed several differences in actomyosin distribution and apoptotic nucleus dynamics, which may indicate fundamental differences in the cellular mechanisms between the two model systems. While in bird embryos, the actomyosin cable spans the whole apico-basal axis of the apoptotic cell and contacts the nucleus all along its apico-basal length; in *Drosophila*, the actomyosin cable only contacts the most apical part of the nucleus. These different types of attachment could represent two different ways to create resistance to the contraction of the cable. It reveals the existence of two different cellular organizations able to generate the apoptotic force in Drosophila and in avians, respectively. Consistently, nuclear upward movement is different between the two species, with a linear movement in avian embryos and a biphasic movement in Drosophila (Ambrosini et al., 2019). Altogether, these data lead us to speculate that even though the cellular processes involved have slightly evolved, apoptotic cells have conserved the capacity to mechanically participate in morphogenesis.

Apoptotic force transmission through a "ratchet-like" mechanism

Importantly, through this transient force, apoptotic cells transmit a mechanical signal to their neighbors in order to make them change their shape. The cellular mechanism involved was not identified in *Drosophila* (Monier et al., 2015). However, in birds, we show that this mechanical cascade relies on the transient generation of an apico-basal pulling force by apoptotic cells, which is sensed and memorized by their neighbors through the persistence of apical deformations and local cell rearrangement long after cell fragmentation. Thus, the mechanical impact of each apoptotic cell is partly maintained through the local bending of the epithelium. Thus, the apoptotic cells that are highly present in the dorsolateral area of the epithelium would collectively impact the surrounding tissue by a "ratchet-like" mechanism and lead to the progressive bending of the epithelium (Figure 4H).

Limitations of the study

Thus, apopototic cells, while still strongly integrated in the neuroepithelium, impact the local organization of the tissue (rosette formation and apical deformation). Unfortunately, since the apical surface of the neuroepithelium becomes rapidly inaccessible during tube closure (see Video S1), we were unable to track cell rearrangement during the whole bending of the DLHP and characterize the topological memory of the apoptotic force in more detail. Also, although the inhibition of apoptosis perturbed

apoptotic cell before pulling, at pulling peak, and at fragmentation. The apical surface recovers its initial position after 25′ at early stages (1–3 ss), whereas it does not at later stages (4–6 ss).

(B) Dot plot quantification of the angle of apical deformation of apoptotic cells before pulling, at the peak of apical pulling and at fragmentation.

(C) Dot plot quantification of the speed of apical pulling or release.

(D) Dot plot quantification of the time between the start and the peak of pulling (start peak) and the time between the peak of pulling and the fragmentation (peak fragmentation).

(E and F) Cell orientation changes at the vicinity of control cells (E) or constricting apoptotic cells (F) in quail embryos transgenic for cytoskeletal markers. Raw images and cross sections are shown in Figure S4. Outline of the first row of neighbors in representative examples (upper panel); scheme showing the control or apoptotic reference cells in green and the orientation of neighboring cells by the black lines at maximal apical constriction (T0), 15′ before (−T15′) and 15′ after (+T15′) (middle panel). Quantification of the orientation of the 1st row of neighbors (lower panel). 0° indicates a perfect radial orientation.

(G) Distribution of apical myosin II along the DV axis of the neural tube.

(H) Model of the apoptotic force impact in vertebrates neuroepithelium. Actomyosin accumulates underneath a basally located nucleus. An apico-basal cable is formed and is linked to the nucleus. The apoptotic force drives apical and the basal deformations of the epithelium and basal deformation of the nucleus. The nucleus blebs during its upward movement and fragments when it reaches the apical side, which coincides with basal detachment and apical release. Apoptotic cell neighbors keep a topological memory of the apoptotic force exerted, which, cumulatively, impacts tissue dynamics and participates in the active bending of the dorsal part of the neural tube.

neuroepithelium bending, it did not completely prevent neural tube closure. This strongly suggests that other mechanisms are at play in this large-scale tissue reorganization.

STAR★METHODS

Detailed methods are provided in the online version of this paper and include the following:

- KEY RESOURCES TABLE
- RESOURCE AVAILABILITY
  - Lead contact
  - Materials availability
  - Data and code availability
- EXPERIMENTAL MODEL AND SUBJECT DETAILS
  - Experimental animals
- METHOD DETAILS
  - Drug treatment
  - Electroporation
  - Immunofluorescence
  - Microscopy of fixed samples
  - Time lapse microscopy
  - Laser ablation
- QUANTIFICATION AND STATISTICAL ANALYSIS
  - Image processing and analysis
  - Position and angle of DLHP
  - Distribution of apoptosis along DV axis of neuroepithelium
  - Quantification of effectiveness of QVD-OPh treatment
  - Measurements of apical and basal surface straightness
  - Position, displacement and velocity of nuclei
  - Nucleus fragmentation time
  - Nucleus deformation
  - Cell Orientation measurements
  - Quantification of apical myosin
  - Statistical analysis and graphs
  - Statistical significance

SUPPLEMENTAL INFORMATION

Supplemental information can be found online at https://doi.org/10.1016/j.devcel.2022.02.020.

ACKNOWLEDGMENTS

We thank Eric Theveneau, Alice Davy, Corinne Benassayag, and Bruno Monier for their constructive comments on the manuscript. M.S.'s lab is supported by grants from the European Research Council (ERC) under the European Union Horizon 2020 research and innovation program (grant number EPAF: 648001), from the Institut National de la Santé et de la Recherche Médicale (Inserm, Plan cancer 2014–2019), and from the association Toulouse Cancer Santé (TCS, ApoMacImaging: 171441). S.T. had a CIFRE fellowship from the ANRT and now has a fellowship from the Fondation pour la Recherche Médicale (FRM). The transgenic quail lines used in this project were generated thanks to the European Research Council under the European Union's Seventh Framework Programme (FP7/2007-2013) and ERC grant agreement no: 337635 to J.G.

AUTHOR CONTRIBUTIONS

D.R. conceived and performed all the experiments in avian embryos. S.T. participated in data analysis regarding cell stretching around apoptotic cells. A.P. participated in data analysis regarding the apoptotic pattern. B.B. helped with time-lapse imaging of apoptosis in whole-mount embryos on a Zeiss Axio-Imager, and G.A. post-processed these time-lapse movies. J.G. generated the quail line with cytoskeletal fluorescent markers. D.R. and M.S. wrote the paper. M.S. supervised the project and provided the funding.

DECLARATION OF INTERESTS

The authors declare no competing interests.

Received: April 16, 2021
Revised: November 15, 2021
Accepted: February 22, 2022
Published: March 17, 2022

REFERENCES

Ainsworth, S.J., Stanley, R.L., and Evans, D.J. (2010). Developmental stages of the Japanese quail. J. Anat. *216*, 3–15. https://doi.org/10.1111/j.1469-7580.2009.01173.x.

Ambrosini, A., Rayer, M., Monier, B., and Suzanne, M. (2019). Mechanical function of the nucleus in force generation during epithelial morphogenesis. Dev. Cell *50*, 197–211.e5. https://doi.org/10.1016/j.devcel.2019.05.027.

Bindels, D.S., Haarbosch, L., van Weeren, L., Postma, M., Wiese, K.E., Mastop, M., Aumonier, S., Gotthard, G., Royant, A., Hink, M.A., and Gadella, T.W. (2017). mScarlet: A bright monomeric red fluorescent protein for cellular imaging. Nat. Methods *14*, 53–56. https://doi.org/10.1038/nmeth.4074.

Cecconi, F., Alvarez-Bolado, G., Meyer, B.I., Roth, K.A., and Gruss, P. (1998). Apaf1 (CED-4 homolog) regulates programmed cell death in mammalian development. Cell *94*, 727–737. https://doi.org/10.1016/s0092-8674(00)81732-8.

Chanet, S., and Martin, A.C. (2014). Mechanical force sensing in tissues. Prog. Mol. Biol. Transl. Sci. *126*, 317–352. https://doi.org/10.1016/B978-0-12-394624-9.00013-0.

Chapman, S.C., Collignon, J., Schoenwolf, G.C., and Lumsden, A. (2001). Improved method for chick whole-embryo culture using a filter paper carrier. Dev. Dyn. *220*, 284–289. https://doi.org/10.1002/1097-0177(20010301)220:3<284::AID-DVDY1102>3.0.CO;2-5.

Chertkova, A.O., Mastop, M., P.M., van Bommel, N., van der Niet, S., Batenburg, K.L., Joosen, L., Gadella, T.W.J., Okada, Y., and Goedhart, J. Robust and bright genetically encoded fluorescent markers for highlighting structures and compartments in mammalian cells. Preprint at bioRxiv.

Copp, A.J., and Greene, N.D. (2010). Genetics and development of neural tube defects. J. Pathol. *220*, 217–230. https://doi.org/10.1002/path.2643.

Davidson, L.A. (2012). Epithelial machines that shape the embryo. Trends Cell Biol. *22*, 82–87. https://doi.org/10.1016/j.tcb.2011.10.005.

Elms, P., Siggers, P., Napper, D., Greenfield, A., and Arkell, R. (2003). Zic2 is required for neural crest formation and hindbrain patterning during mouse development. Dev. Biol. *264*, 391–406. https://doi.org/10.1016/j.ydbio.2003.09.005.

Fuchs, Y., and Steller, H. (2011). Programmed cell death in animal development and disease. Cell *147*, 742–758. https://doi.org/10.1016/j.cell.2011.10.033.

Gibson, A., Robinson, N., Streit, A., Sheng, G., and Stern, C.D. (2011). Regulation of programmed cell death during neural induction in the chick embryo. Int. J. Dev. Biol. *55*, 33–43. https://doi.org/10.1387/ijdb.103233sg.

Gracia, M., Theis, S., Proag, A., Gay, G., Benassayag, C., and Suzanne, M. (2019). Mechanical impact of epithelial-mesenchymal transition on epithelial morphogenesis in Drosophila. Nat. Commun. *10*, 2951. https://doi.org/10.1038/s41467-019-10720-0.

Häcker, G. (2000). The morphology of apoptosis. Cell Tissue Res. *301*, 5–17.

Hakem, R., Hakem, A., Duncan, G.S., Henderson, J.T., Woo, M., Soengas, M.S., Elia, A., de la Pompa, J.L., Kagi, D., Khoo, W., et al. (1998). Differential requirement for caspase 9 in apoptotic pathways in vivo. Cell *94*, 339–352. https://doi.org/10.1016/s0092-8674(00)81477-4.

Hamburger, V., and Hamilton, H.L. (1951). A series of normal stages in the development of the chick embryo. J. Morphol. *88*, 49–92.

Heisenberg, C.P., and Bellaïche, Y. (2013). Forces in tissue morphogenesis and patterning. Cell *153*, 948–962. https://doi.org/10.1016/j.cell.2013.05.008.

Hernández-Martínez, R., and Covarrubias, L. (2011). Interdigital cell death function and regulation: New insights on an old programmed cell death model. Dev. Growth Differ. *53*, 245–258. https://doi.org/10.1111/j.1440-169X.2010.01246.x.

Hirata, M., and Hall, B.K. (2000). Temporospatial patterns of apoptosis in chick embryos during the morphogenetic period of development. Int. J. Dev. Biol. *44*, 757–768.

Honarpour, N., Gilbert, S.L., Lahn, B.T., Wang, X., and Herz, J. (2001). Apaf-1 deficiency and neural tube closure defects are found in fog mice. Proc. Natl. Acad. Sci. USA *98*, 9683–9687. https://doi.org/10.1073/pnas.171283198.

Houde, C., Banks, K.G., Coulombe, N., Rasper, D., Grimm, E., Roy, S., Simpson, E.M., and Nicholson, D.W. (2004). Caspase-7 expanded function and intrinsic expression level underlies strain-specific brain phenotype of caspase-3-null mice. J. Neurosci. *24*, 9977–9984. https://doi.org/10.1523/JNEUROSCI.3356-04.2004.

Kerr, J.F., Wyllie, A.H., and Currie, A.R. (1972). Apoptosis: A basic biological phenomenon with wide-ranging implications in tissue kinetics. Br. J. Cancer *26*, 239–257.

Kinoshita, N., Sasai, N., Misaki, K., and Yonemura, S. (2008). Apical accumulation of Rho in the neural plate is important for neural plate cell shape change and neural tube formation. Mol. Biol. Cell *19*, 2289–2299. https://doi.org/10.1091/mbc.e07-12-1286.

Kuida, K., Haydar, T.F., Kuan, C.Y., Gu, Y., Taya, C., Karasuyama, H., Su, M.S., Rakic, P., and Flavell, R.A. (1998). Reduced apoptosis and cytochrome c-mediated caspase activation in mice lacking caspase 9. Cell *94*, 325–337. https://doi.org/10.1016/s0092-8674(00)81476-2.

Kuida, K., Zheng, T.S., Na, S., Kuan, C., Yang, D., Karasuyama, H., Rakic, P., and Flavell, R.A. (1996). Decreased apoptosis in the brain and premature lethality in CPP32-deficient mice. Nature *384*, 368–372. https://doi.org/10.1038/384368a0.

Lecuit, T., Lenne, P.F., and Munro, E. (2011). Force generation, transmission, and integration during cell and tissue morphogenesis. Annu. Rev. Cell Dev. Biol. *27*, 157–184. https://doi.org/10.1146/annurev-cellbio-100109-104027.

Martin, A.C., and Goldstein, B. (2014). Apical constriction: Themes and variations on a cellular mechanism driving morphogenesis. Development *141*, 1987–1998. https://doi.org/10.1242/dev.102228.

Martin, A.C., Kaschube, M., and Wieschaus, E.F. (2009). Pulsed contractions of an actin-myosin network drive apical constriction. Nature *457*, 495–499. https://doi.org/10.1038/nature07522.

Massa, V., Savery, D., Ybot-Gonzalez, P., Ferraro, E., Rongvaux, A., Cecconi, F., Flavell, R., Greene, N.D., and Copp, A.J. (2009). Apoptosis is not required for mammalian neural tube closure. Proc. Natl. Acad. Sci. USA *106*, 8233–8238. https://doi.org/10.1073/pnas.0900333106.

Matsuda, T., and Cepko, C.L. (2007). Controlled expression of transgenes introduced by in vivo electroporation. Proc. Natl. Acad. Sci. USA *104*, 1027–1032. https://doi.org/10.1073/pnas.0610155104.

McShane, S.G., Molè, M.A., Savery, D., Greene, N.D., Tam, P.P., and Copp, A.J. (2015). Cellular basis of neuroepithelial bending during mouse spinal neural tube closure. Dev. Biol. *404*, 113–124. https://doi.org/10.1016/j.ydbio.2015.06.003.

Mitchell, L.E. (2005). Epidemiology of neural tube defects. Am. J. Med. Genet. *135C*, 88–94. https://doi.org/10.1002/ajmg.c.30057.

Monier, B., Gettings, M., Gay, G., Mangeat, T., Schott, S., Guarner, A., and Suzanne, M. (2015). Apico-basal forces exerted by apoptotic cells drive epithelium folding. Nature *518*, 245–248. https://doi.org/10.1038/nature14152.

Morriss-Kay, G.M. (1981). Growth and development of pattern in the cranial neural epithelium of rat embryos during neurulation. J. Embryol. Exp. Morphol. *65* (suppl), 225–241.

Nakaya, Y., Sukowati, E.W., Wu, Y., and Sheng, G. (2008). RhoA and microtubule dynamics control cell-basement membrane interaction in EMT during gastrulation. Nat. Cell Biol. *10*, 765–775. https://doi.org/10.1038/ncb1739.

Nikolopoulou, E., Galea, G.L., Rolo, A., Greene, N.D., and Copp, A.J. (2017). Neural tube closure: Cellular, molecular and biomechanical mechanisms. Development *144*, 552–566. https://doi.org/10.1242/dev.145904.

Nishimura, T., Honda, H., and Takeichi, M. (2012). Planar cell polarity links axes of spatial dynamics in neural-tube closure. Cell *149*, 1084–1097. https://doi.org/10.1016/j.cell.2012.04.021.

Nishimura, T., and Takeichi, M. (2008). Shroom3-mediated recruitment of Rho kinases to the apical cell junctions regulates epithelial and neuroepithelial planar remodeling. Development *135*, 1493–1502. https://doi.org/10.1242/dev.019646.

Pearl, E.J., Li, J., and Green, J.B. (2017). Cellular systems for epithelial invagination. Philos. Trans. R. Soc. Lond. B Biol. Sci. *372*. https://doi.org/10.1098/rstb.2015.0526.

Pérez-Garijo, A., Fuchs, Y., and Steller, H. (2013). Apoptotic cells can induce non-autonomous apoptosis through the TNF pathway. eLife *2*, e01004. https://doi.org/10.7554/eLife.01004.

Roellig, D., Tan-Cabugao, J., Esaian, S., and Bronner, M.E. (2017). Dynamic transcriptional signature and cell fate analysis reveals plasticity of individual neural plate border cells. eLife *6*. https://doi.org/10.7554/eLife.21620.

Romanos, M., Allio, G., Roussigné, M., Combres, L., Escalas, N., Soula, C., Médevielle, F., Steventon, B., Trescases, A., and Bénazéraf, B. (2021). Cell-to-cell heterogeneity in Sox2 and Bra expression guides progenitor motility and destiny. eLife *10*. https://doi.org/10.7554/eLife.66588.

Saadaoui, M., Rocancourt, D., Roussel, J., Corson, F., and Gros, J. (2020). A tensile ring drives tissue flows to shape the gastrulating amniote embryo. Science *367*, 453–458. https://doi.org/10.1126/science.aaw1965.

Sauka-Spengler, T., and Barembaum, M. (2008). Gain- and loss-of-function approaches in the chick embryo. Methods Cell Biol. *87*, 237–256. https://doi.org/10.1016/S0091-679X(08)00212-4.

Schoenwolf, G.C. (1985). Shaping and bending of the avian neuroepithelium: morphometric analyses. Dev. Biol. *109*, 127–139. https://doi.org/10.1016/0012-1606(85)90353-7.

Schoenwolf, G.C., and Franks, M.V. (1984). Quantitative analyses of changes in cell shapes during bending of the avian neural plate. Dev. Biol. *105*, 257–272. https://doi.org/10.1016/0012-1606(84)90284-7.

Schott, S., Ambrosini, A., Barbaste, A., Benassayag, C., Gracia, M., Proag, A., Rayer, M., Monier, B., and Suzanne, M. (2017). A fluorescent toolkit for spatiotemporal tracking of apoptotic cells in living Drosophila tissues. Development *144*, 3840–3846. https://doi.org/10.1242/dev.149807.

Sherrard, K., Robin, F., Lemaire, P., and Munro, E. (2010). Sequential activation of apical and basolateral contractility drives ascidian endoderm invagination. Curr. Biol. *20*, 1499–1510. https://doi.org/10.1016/j.cub.2010.06.075.

Smith, J.L., and Schoenwolf, G.C. (1988). Role of cell-cycle in regulating neuroepithelial cell shape during bending of the chick neural plate. Cell Tissue Res. *252*, 491–500. https://doi.org/10.1007/BF00216636.

Smith, J.L., and Schoenwolf, G.C. (1989). Notochordal induction of cell wedging in the chick neural plate and its role in neural tube formation. J. Exp. Zool. *250*, 49–62. https://doi.org/10.1002/jez.1402500107.

Smith, J.L., Schoenwolf, G.C., and Quan, J. (1994). Quantitative analyses of neuroepithelial cell shapes during bending of the mouse neural plate. J. Comp. Neurol. *342*, 144–151. https://doi.org/10.1002/cne.903420113.

Sui, L., Alt, S., Weigert, M., Dye, N., Eaton, S., Jug, F., Myers, E.W., Jülicher, F., Salbreux, G., and Dahmann, C. (2018). Differential lateral and basal tension drive folding of Drosophila wing discs through two distinct mechanisms. Nat. Commun. *9*, 4620. https://doi.org/10.1038/s41467-018-06497-3.

Sui, L., and Dahmann, C. (2020). Increased lateral tension is sufficient for epithelial folding in Drosophila. Development *147*. https://doi.org/10.1242/dev.194316.

Sullivan-Brown, J., and Goldstein, B. (2012). Neural tube closure: The curious case of shrinking junctions. Curr. Biol. *22*, R574–R576. https://doi.org/10.1016/j.cub.2012.06.048.

Suzanne, M., Petzoldt, A.G., Spéder, P., Coutelis, J.B., Steller, H., and Noselli, S. (2010). Coupling of apoptosis and L/R patterning controls stepwise organ looping. Curr. Biol. *20*, 1773–1778. https://doi.org/10.1016/j.cub.2010.08.056.

Toyama, Y., Peralta, X.G., Wells, A.R., Kiehart, D.P., and Edwards, G.S. (2008). Apoptotic force and tissue dynamics during Drosophila embryogenesis. Science *321*, 1683–1686. https://doi.org/10.1126/science.1157052.

Uehata, M., Ishizaki, T., Satoh, H., Ono, T., Kawahara, T., Morishita, T., Tamakawa, H., Yamagami, K., Inui, J., Maekawa, M., and Narumiya, S. (1997). Calcium sensitization of smooth muscle mediated by a Rho-associated protein kinase in hypertension. Nature *389*, 990–994. https://doi.org/10.1038/40187.

Umetsu, D., and Kuranaga, E. (2017). Planar polarized contractile actomyosin networks in dynamic tissue morphogenesis. Curr. Opin. Genet. Dev. *45*, 90–96. https://doi.org/10.1016/j.gde.2017.03.012.

Urase, K., Kouroku, Y., Fujita, E., and Momoi, T. (2003). Region of caspase-3 activation and programmed cell death in the early development of the mouse forebrain. Brain Res. Dev. Brain Res. *145*, 241–248. https://doi.org/10.1016/j.devbrainres.2003.07.002.

Wei, L., Roberts, W., Wang, L., Yamada, M., Zhang, S., Zhao, Z., Rivkees, S.A., Schwartz, R.J., and Imanaka-Yoshida, K. (2001). Rho kinases play an obligatory role in vertebrate embryonic organogenesis. Development *128*, 2953–2962.

Weil, M., Jacobson, M.D., and Raff, M.C. (1997). Is programmed cell death required for neural tube closure? Curr. Biol. *7*, 281–284.

Yamaguchi, Y., Shinotsuka, N., Nonomura, K., Takemoto, K., Kuida, K., Yosida, H., and Miura, M. (2011). Live imaging of apoptosis in a novel transgenic mouse highlights its role in neural tube closure. J. Cell Biol. *195*, 1047–1060. https://doi.org/10.1083/jcb.201104057.

Yang, Q., Roiz, D., Mereu, L., Daube, M., and Hajnal, A. (2017). The invading anchor cell induces lateral membrane constriction during vulval lumen morphogenesis in C. elegans. Dev. Cell *42*, 271–285.e3. https://doi.org/10.1016/j.devcel.2017.07.008.

Ybot-Gonzalez, P., Gaston-Massuet, C., Girdler, G., Klingensmith, J., Arkell, R., Greene, N.D., and Copp, A.J. (2007). Neural plate morphogenesis during mouse neurulation is regulated by antagonism of Bmp signalling. Development *134*, 3203–3211. https://doi.org/10.1242/dev.008177.

Yoshida, H., Kong, Y.Y., Yoshida, R., Elia, A.J., Hakem, A., Hakem, R., Penninger, J.M., and Mak, T.W. (1998). Apaf1 is required for mitochondrial pathways of apoptosis and brain development. Cell *94*, 739–750. https://doi.org/10.1016/s0092-8674(00)81733-x.

Zhang, J., Wang, X., Cui, W., Wang, W., Zhang, H., Liu, L., Zhang, Z., Li, Z., Ying, G., Zhang, N., and Li, B. (2013). Visualization of caspase-3-like activity in cells using a genetically encoded fluorescent biosensor activated by protein cleavage. Nat. Commun. *4*, 2157. https://doi.org/10.1038/ncomms3157.

STAR★METHODS

KEY RESOURCES TABLE

Reagent or resource	Source	Identifier
Antibodies		
rabbit cleaved Caspase3 (D175) (1:100)	Cell Signalling Technologies	Cat#9661S; RRID: AB_2341188
rabbit anti-pMyosin light chain 2 (1:50)	Cell Signalling Technologies	Cat#3671S; RRID: AB_330248
mouse anti-nuclear Lamins II/III (1:10)	Developmental Studies Hybridoma Bank (DSHB), gift from Eric Theveneau lab	Cat#14a9; RRID: AB_531882
mouse monoclonal anti-CTNNA1 [1G5] (1:100)	Abcam	Cat#ab231306
mouse monoclonal anti-phospho-Histone yH2Ax (Ser139) clone JBW301 (1:500)	Sigma-Aldrich, gift from Gaelle Legube lab	Cat##05-636; RRID: AB_309864
chicken anti-laminin-1 (1:50)	DSHB	Cat#3H11; RRID: AB_528342
Goat anti-rabbit IgG 488	Molecular Probes	Cat#A-11034; RRID: AB_2576217
Goat anti-rabbit IgG 546	Molecular Probes	Cat#A-11035; RRID: AB_143051
Goat anti-mouse IgG 488	Molecular Probes	Cat# A-11001; RRID: AB_2534069
Goat anti-mouse IgG 555	Molecular Probes	Cat# A-21422; RRID: AB_141822
Chemicals, peptides, and recombinant proteins		
Phalloidin-Rhodamine	Invitrogen	Cat#R415
Phalloidin 647	Interchim	Cat#FP-BZ9630
DMSO	Sigma-Aldrich	Cat#D8418
Hoechst 33342	Sigma-Aldrich	Cat#B2883
QVD-Oph	Selleckchem	Cat#S7311
QVD-Oph	MedChemExpress	Cat#HY-12305
Y27632	Sigma-Aldrich	Cat#Y0503
Difco Agar Noble, powder	BD	Cat#214230
Triton-X 100	Sigma-Aldrich	Cat#X100-1L
Deposited data		
Github	https://github.com/suzannelab/AvianNeuralTubeBending	https://doi.org/10.5281/zenodo.6140952
Experimental models: Organisms/strains		
Eggs Gallus gallus	Société Scal 39, ZI des Poumarderes, 32600 L'Isle Jourdain, France	N/A
Eggs Coturnix japonica	Cailles de Chanteloup 104, Le Vélobert, 35150 Corps-Nuds, France	N/A
Quail embryos transgenic for cytoskeletal markers	(Saadaoui et al., 2020)	Institut Pasteur Paris
Quail embryos transgenic for memGFP	(Saadaoui et al., 2020)	Institut Pasteur Paris
Oligonucleotides		
Primer GC3Ai-for 5′- GCTTGATATCGAATTCTAGCGAATT GCCACCATGTACC-3′	This study	N/A
Primer GC3Ai-rev 5′-GAGTGAGTCGCGGCCGCTTACAG GTCC-3′	This study	N/A

(*Continued on next page*)

Continued

Reagent or resource	Source	Identifier
Primer PalmitoGap43-for 5'- CGTCAGATCCGCTAGCCGGTCGC CACCATGC-3'	This study	N/A
Primer PalmitoGap43-rev 5'-GACCGGTAGCGCTAGCTTTTCA ACCTGTTTGGTTCTTCTCA-3'	This study	N/A
Recombinant DNA		
Plasmid: pLifeAct_Scarlet_N1	(Bindels et al., 2017)	Addgene plasmid RRID:Addgene_85054
Plasmid: 3xnls-mScarlet-I	*(*Chertkova et al.*) 160374* 10.1101/160374	Addgene plasmid RRID:Addgene_98816
Plasmid: tdTomato-LC Myosin-N-7	Gift from Michael Davidson	Addgene plasmid RRID:Addgene_58108
Plasmid: pCAG-mGFP	(Matsuda and Cepko, 2007)	Addgene plasmid RRID:Addgene_14757
Plasmid: pmScarlet-i-C1	(Bindels et al., 2017)	Addgene plasmid RRID:Addgene_85054
Plasmid: DN-RhoA	gift from Guojun Sheng lab; Nakaya et al. (2008)	IRCMS - Kumamoto University
Plasmid: H2B-GFP	gift from B. Bénazéraf Lab	CBI Toulouse
Plasmid: memScarlet	This study	N/A
Plasmid: pGC3Ai	This study	N/A
Plasmid: pCIG	gift from Fabienne Pituello Lab	CBI Toulouse
cDNA: GC3Ai	a gift from Binghui Li's Lab; (Zhang et al., 2013)	Tianjin Medical University Cancer Institute and Hospital, China
Software and algorithms		
GraphPad Prism 8	GraphPad Software	RRID: SCR_002798
Adobe Illustrator CS6	Adobe	RRID:SCR_010279
Imaris 9.2.1	Bitplane	RRID:SCR_007370
Fiji	https://fiji.sc/	RRID: SCR_002285
SnapGene	GSL Biotech LLC	RRID:SCR_015052
ZEN Black	ZEISS	RRID: SCR_018163
ZEN Blue	ZEISS	RRID: SCR_013672
ROE Syscon	Rapp OptoElectronic	N/A
Microscopes		
Confocal LSM880 with Airyscan	ZEISS	54477; RRID:SCR_020925
Confocal LSM900 Airy 2	ZEISS	56137
Objective LD C-Apochromat 40X/1.1 W Korr	ZEISS	421867-9970-000
Objective Plan-Apochromat 40X/1.3 Oil	ZEISS	420762-9800-799
Objective Plan-Apochromat 40X/1.4 Oil	ZEISS	420762-9900-000
Objective Plan-Apochromat 63X/1.4 Oil	ZEISS	420782–9900
Pulsed Laser 532nm	Rapp-opto	DPSL 532/42/CLS, UGA-42 Firefly
Axio Imager type 2	ZEISS	RRID:SCR_018876
Objective 20X/0.8 dry	ZEISS	420650-9902-000

RESOURCE AVAILABILITY

Lead contact

Further information and requests for resources and reagents should be directed to and will be fulfilled by the lead contact, Magali Suzanne (magali.suzanne@univ-tlse3.fr).

Materials availability

All stable reagents generated in this study are available from the lead contact without restriction.

Data and code availability

- Accession numbers are listed in the key resources table. Microscopy data reported in this paper will be shared by the lead contact upon request.
- Any additional information required to reanalyze the data reported in this paper is available from the lead contact upon request.
- All original code has been deposited In Github and is publicly available as of the date of publication (https://github.com/suzannelab/AvianNeuralTubeBending and DOI https://doi.org/10.5281/zenodo.6140952).

EXPERIMENTAL MODEL AND SUBJECT DETAILS

Experimental animals

Wildtype fertilized eggs of chicken (Gallus gallus) and quail (Coturnix japonica) were obtained from commercial sources and incubated at 38.5°C to the desired stages according to embryo development tables for chicken (Hamburger and Hamilton, 1951) and quail (Ainsworth et al., 2010). Embryos were grown ex ovo using the EC culture technique (Chapman et al., 2001). Quail transgenic for membrane-bound GFP or cytoskeleton markers (acto-myosin) were previously described (Saadaoui et al., 2020). Transgenic embryos were collected at the desired stage and transferred to agar/albumen plates.

METHOD DETAILS

Drug treatment

Embryos were collected with ventral side up at HH5-7. QVD-OPh (Selleckchem # S7311, MedChemExpress #HY-12305, diluted in 100% DMSO) was delivered either by pipetting a 20µl drop containing 100-400mM QVD-OPh in 1xPBS on top of embryo or by transferring embryos to agar/albumen plates containing 100-200mM QVD-OPh. Control embryos were treated with 0.5-1.0% DMSO correspondingly. Embryos were incubated until they had reached 5-8 ss and fixed. Note that the duration of the incubation and the repartition of developmental stages was similar for control and QVD-OPh treated embryos (n=26/70 and 22/60 for 5ss; n=26/70 and 16/60 for 6ss; n=12/70 and 14/60 for 7ss and n=6/70 and 8/60 for 8ss, for control (DMSO) and QVD-OPh respectively. Y27632 (Sigma-Aldrich #Y0503; diluted to 1mM stock in ddH_2O according to manufacturer's instructions) was delivered either by pipetting a 20µl drop containing 100µM Y27632 in 1xPBS on top of the embryo or by transferring embryos to agar/albumen plates containing 20-100 µM Y27632. All plates were prewarmed to 38.5°C before drug treatment and embryos were incubated with Y27632 30-60 min before imaging on the imaging stage. Y27632 caused detachment of a great number of cells in all concentrations used. We only considered cells that were still apically and basally attached for our analysis.

Electroporation

Embryos were collected ex ovo at stage HH4-6 and DNA solution was microinjected between the vitelline membrane and the epiblast at the level of the future trunk neural plate. With electrodes positioned on the ventral and dorsal side of the embryo, electroporations were performed as previously described (Sauka-Spengler and Barembaum, 2008) with five 50msec pulses of 4.8V at 100msec intervals. Embryos were incubated at 38.5°C to the desired stage. Electroporated constructs were: pLifeAct_Scarlet_N1 (Bindels et al., 2017) (0.5-0.7µg/µl; gift from Dorus Gadella; Addgene #85054; http://n2t.net/addgene:85054), 3xnls-mScarlet-I (Chertkova AO et al., bioRxiv) (0.5-0.7µg/µl; gift from Dorus Gadella; Addgene #98816; http://n2t.net/addgene:98816), tdTomato-LC Myosin-N-7 (1.0-1.2µg/µl; gift from Michael Davidson; Addgene #58108; http://n2t.net/addgene:58108), H2B-GFP (0.5-0.7 µg/µl; gift from B. Bénazéraf Lab) and membrane-bound GFP (Matsuda and Cepko, 2007) (pCAG-mGFP; addgene #14757, gift from Connie Cepko; http://n2t.net/addgene:14757). *DN-RhoA* construct (Nakaya et al., 2008) (2µg/µl; gift from Guojun Sheng) caused partial detachment of a great number of cells. We only considered cells that were still apically and basally attached for our analysis. Avian GC3Ai expression vector was created as follows: GC3Ai cDNA (Zhang et al., 2013) (a gift from Binghui Li's Lab, Tianjin Medical University Cancer Institute and Hospital, China) was amplified by PCR with primers (GC3Ai-for 5'- GCTTGATATCGAATTCTAGC GAATTGCCACCATGTACC-3'; GC3Ai-rev 5'-GAGTGAGTCGCGGCCGCTTACAGGTCC-3') designed by Snapgene (GSL Biotech LLC; www.snapgene.com) and ligated into EcoR1/Not1 digested pCIG vector containing CMV promoter (gift from F. Pituello Lab) using InFusion cloning. 1µg/µl was used for electroporations. memScarlet expression vector was created as follows: the palmitoylation signal of Gap43 was PCR-amplified from pCAG-mGFP with primers (PalmitoGap43-for 5'- CGTCAGATCCGCTAGCCGG TCGCCACCATGC-3'; PalmitoGap43-rev 5'-GACCGGTAGCGCTAGCTTTTCAACCTGTTTGGTTCTTCTCA-3') designed by Snapgene (GSL Biotech LLC; www.snapgene.com) and ligated into Nhe1 digested pmScarlet-i-C1 vector (Bindels et al., 2017) (addgene 85044; gift from Dorus Gadella;http://n2t.net/addgene:85044; RRID:Addgene_85044) using InFusion cloning. 0.5-0.7µg/µl was used for electroporation.

Immunofluorescence

Embryos were collected at the desired stage and fixed in 4% Paraformaldehyde/1xPBS for 1h at room temperature or 4°C overnight. Embryos were permeabilized in 1xPBS/1% Triton-X 100 for 2x 10min on roller before blocking in 1xPBS/0.2% Triton-X 100/10% goat serum for at least 2h at room temperature and then incubated in primary antibody solution in 1xPBS/0.2% Triton-X 100 for 3 days at 4°C on a roller. Embryos were rinsed 2x and then washed 4x for 15 min in 1xPBS/0.2% Triton-X 100 before secondary antibody solution was added and incubated overnight at 4°C. Finally, embryos were washed as before and then cleared by incubating them in 50% Glucose/1xPBS for at least 2 hours and subsequently in 80% Glucose/1xPBS overnight on a roller. Primary antibodies used were cleaved Caspase3 (D175) (1:100; CST #9661S), rabbit anti-pMyosin light chain 2 (1:50; CST 3671S), mouse anti-nuclear Lamins II/III (1:10; DSHB #14a9; gift from Eric Theveneau lab), mouse monoclonal anti-CTNNA1 [1G5] (1:100; abcam; # ab231306), mouse monoclonal anti-phospho-Histone γH2Ax (Ser139) clone JBW301 (1:500; Sigma-Aldrich #05-636; gift from Gaelle Legube lab) and chicken anti-laminin-1 (1:50; 3H11 was deposited to the DSHB by Halfter, W.M.). Secondary antibodies (Alexa488, Alexa546, Alexa555; Molecular Probes) were used at dilutions of 1:500 to 1:1000. Rhodamine-Phalloidin (1:50; Invitrogen, # R415), Phalloidin-647 (1:50, Interchim, #FP-BZ9630) and Hoechst 33342 (1:1000; Sigma-Aldrich Cat#B2883, 25mg/ml) were added to primary and secondary antibody solutions.

Microscopy of fixed samples

Embryos were mounted on microscopy slides in 80% Glucose/1xPBS confined in an adhesive spacer (rectangle cut in electrical tape) and covered with a 1.5x glass cover slip (Zeiss) with dorsal side up. Embryos were imaged on an inverted LSM880 or LSM900 confocal microscope (Zeiss) with a Plan-Apochromat 63x/1.40 Oil M27, Plan-Apochromat 40x/1.3 Oil or Plan-Apochromat 40x/1.4 Oil objectives. Embryos used in QVD-OPh experiments were imaged using a Plan-Apochromat 10x/0.45 M27 objective on a LSM880 scope. Antero-posterior distribution of apoptosis in the trunk of the embryo was acquired on a Leica DM6000 B microscope (light source Lumencor SOLA light, Roper Scientific CoolSNAP HQ2 CCD camera, MetaMorph 7.8.10 software) using a 2.5x objective or a Zeiss Axio-Imager type 2 (Colibri 8 multi-diode light source) with a 10x objective.

Time lapse microscopy

Transgenic or electroporated embryos were screened for presence of fluorescence and normal morphology and then transferred to two-well Lab-Tek II chambered #1.5 German cover glass slides (Thermo Fisher Scientific #155379) containing 400μl Agar/Albumen as described previously (Roellig et al., 2017). Embryos were imaged at 38.5°C on an inverted Zeiss LSM880 confocal microscope equipped with a piezo stage using a LD C-Apochromat 40x/1.1 W Korr M27 objective and Fast Airyscan mode at time intervals of 60-90sec. Snapshot shown in Figure S1E was imaged with a 20X objective on a Zeiss Axio-Imager type 2 (Colibri 8 multi-diode light source) equipped with a heat chamber at 38.5°C as previously described (Romanos et al., 2021).

Laser ablation

Laser ablation was performed with a pulsed DPSS laser (532 nm, pulse length 1.5ns, repetition rate up to 1kHz, 3.5μJ/pulse) on a Zeiss LSM 880 laser scanning microscope steered by a galvanometer-based laser scanning device (DPPS-532/UGA-42) from Rapp OptoElectronic, Hamburg,Germany. The laser beam was focused through a 40x water immersion lens (LD C-Apochromat 40x/1.1 W Korr M27 from Zeiss) at a 2x zoom. Photo-disruption was produced in the focal plane by illuminating at 90% laser power a 30-pixel line for about 2.5 sec. Images of quail embryos transgenic for actin and myosin were acquired every 320msec.

QUANTIFICATION AND STATISTICAL ANALYSIS

Image processing and analysis

Images were processed and analyzed with Imaris (Bitplane, version 9.2.1 64x) and Fiji (https://fiji.sc/) software. Images presented in Figure S1E were processed as previously described (Romanos et al., 2021).

Position and angle of DLHP

To define the position of the DLPH in wildetype embryos, a dot (dot function in Fiji) was placed on the DLHP in 6 to 8 somite stage embryos and line was drawn from the MHP (0%) to the fusion point (100%) along the DV axis. With help of a homemade Fiji macro the relative position (%) of the DLHP was then calculated. The average value was 67 % +/− 10%. We used that range to estimate the average of dying cells at the DLHP in Figure 1E. For embryos where neuroepithelium bending had not occurred, the DLHP was predicted to be positioned at two/thirds between the MHP and the fusion point, based on these measurements and whole embryo movies (Figure S1A;Video S1). At the level of the 5th somite pair a two segment line was drawn along the curvature of the epithelium at the DLHP in Fiji (segmented line tool). Using a homemade macro, the angle between the two segments was calculated automatically.

Distribution of apoptosis along DV axis of neuroepithelium

Area of interest was limited to the level of the 4th and 5th somite pair. Within this area, and the help of a homemade Fiji macro, optical transverse sections (75pixel width) of the neuroepithelium were created by using the reslice tool. Dying cells on the left or right side of a section were marked manually using the dot function. We counted only cells that were in the process of dying, based on cell

body shape. Apoptotic fragments were excluded, since they tend to move around in the tissue. A line was drawn from the MHP (0%) to the fusion point (100%) along the left or right side of the neuroepithelium, respectively. Positions of dots and lines were automatically saved for future reference. The relative position of the dots along this line was calculated for left or right side, respectively, and saved. An R script was used to normalize and assemble all data into an Excel work sheet, a Python script to organize the measurements per embryos and somite stages. The corresponding code is available in Github: (https://github.com/suzannelab/AvianNeuralTubeBending).

Quantification of effectiveness of QVD-OPh treatment

In Fiji images of control and QVD-OPh-treated embryos at the 6-7somite stage were cropped at the 2-4 somite pair area using the rectangle tool in Fiji. Rectangle size was kept constant for all embryos. From these crops a single z-slice in the dorsal part of the neural tube at approximately the same level was chosen for every embryo. We chose a single z-slice to facilitate counting of the apoptotic signal. A dot was placed on every anti-Cas3-positive dot using the dot function in Fiji and their number was saved for each embryo.

Measurements of apical and basal surface straightness

Single z-slices at the level of the DLHP were used for these measurements. Using Fiji, a line was drawn tracing the apical and basal surfaces, respectively. A second line was drawn between the extremities of the first lines. By deviding the length of the first line and second line for the apical and the basal side respectively, a ratio of the straightness of the apical and basal surfaces was obtained.

Position, displacement and velocity of nuclei

A ratio was formed by calculating the distance of the center of the nucleus to the basal side divided by the overall apico-basal height of the epithelium. Ratio was calculated for nuclear position at the beginning and the end of displacement. Distances were measured using the Fiji software. Positions of control nuclei were calculated accordingly over a period of 10 time frames, which is the average number of time frames in apoptotic samples. To calculate the mean velocity, we tracked apoptotic nuclei over time between the beginning and end of apoptotic nucleus migration or over 10 time frames for control nuclei using the Fiji Manual Tracking tool. We then divided the displacement per time frame by the interval time (60 to 90sec).

Nucleus fragmentation time

The start frame was chosen when the nucleus was at its basal-most position before upward movement and last frame when the first nuclear fragments became visible. The elapsed time between these two frames calculated.

Nucleus deformation

Using the elipse tool in Fiji and a homemade macro, an elipse was manually fitted to the nucleus before its deformation and at the following time point (start of deformation). Using the line tool, a line was fitted to the elipse in apico-basal direction and a second one perpendicular to it. Then the ratio was formed between these two values.

Cell Orientation measurements

In all movies, embryos have the same orientation (medial left / lateral right). Three different time points have been extracted from these movies. For apoptotic cells: before the beginning of apical constriction (T-15'), at complete apical constriction (T0), and at the same average duration between beginning to complete apical constriction (T+15'). For control cells, time points were chosen at equal intervals. The ROI manager was used to mark the same cell in all frames. By using the fit ellipse tool the anisotropy and cell orientation was calculated as the major/minor ratio defined by fit ellipse tool. In each movie, a central control or apoptotic cell was used as reference. With a homemade python script, we calculated the directional angle of the neighbouring cell to the reference cell. We then calculated the difference between the directional angle and the orientation of the neighbouring cell (the smaller the value, the more the cell is oriented toward the reference cell, see the scheme in Figure S4A).

Quantification of apical myosin

Using the line tool in Fji and with help of a homemade macro a line was drawn along the apical side of the epithelium from the midline to the fusion point and the intensity was measured. A second line was drawn inside the epithelium. To normalize the levels of apical myosin the value of each position along the mediolateral axis was devided by the average value of a second line that was drawn inside the epithlium. We assumed stable myosin levels inside the epithelium. To make the measurements along the apical side comparable (the lines drawn on the apical side were of different lengths) the lines were fitted to a scale of 0 to 100 using a homemade Python script.

Statistical analysis and graphs

Graphs and statistical data were generated in Prism (GraphPad), Excel (Microsoft) or Python. Statistical tests used, N and p values are described in the figure legends. Number of n:

In Figures 1C and,1D: between 10 and 29 transversal sections per embryo (number of embryos at 3ss n=3, 4ss n=4, 5ss n=3, 6ss n=3, 7ss n=3, 8ss n=3). Figures 1H–1L: n=11 and 13 for 5ss; 13 and 8 for 6ss; 6 and 7 for 7ss and 3 and 4 for 8ss, for control and QVD experiment respectively. Figure 2H: n=5 embryos and 20 cuts for the control; 3 embryos and 17 cuts for the cable cut. Figures 3J and

3K: n= 5, 4 and 14, respectively for Y27632, dn-RhoA and control. Figure 3L: n= 5 and 9 for Y27632 and control respectively. Figure 3M: n=4 and 12 for Y27632 and control respectively. Figure 4A: n=11 cells for 1-3ss and 14 cells for 4-6ss. Figure 4B: n=10 cells. Figure 4C: n=14 cells. Figure 4D: n=13 cells. Figures 4E and 4F: 22 apoptotics cells, with 125 neighboring cells from 8 movies and 12 controls cells, with 73 neighboring cells from 7 movies, from 1-3ss embryos. Figure 4G: between 4-8 slices per embryo, 5 embryos total at 3-5ss and between 4-8 slices per embryo, 9 embryos total at 6-8ss.

Box plots:

In Figure 1L: Dotted lines point to average angle of control embryos at the 5 and 7 somite stage to illustrate angle differences over time. In Figures 1L, 3L, 3J, and 3M: The lower and upper quartile represent the 0-100 percentile range.

Dot plots:

In Figures 4B, 4C, and 4D: Error bars = standard deviation.

Histograms:

In Figure 2H: Error bar = standard deviation. Apico-basal cable cut: n = 20 cables in 5 embryos, control lateral cut: n = 17 cables in 3 embryos. ap= apical, b = basal.

Curves:

In Figure 1D: Blue and orange dotted lines = polynomial trendlines (order 6). In Figure 1E: Solid line curves represent the mean; dotted line curves, the standard error of mean. In Figure 3K: Solid line curves represent the mean; dotted line curves, the standard deviation. Black box indicates velocity peak of apoptotic nuclei just before they reach the apical side. In Figure 4A: Solid line curves represent the mean; dotted line curves, the standard deviation. In Figure 4G: Dotted line curves represent the mean; error bars, the standard deviation.

Statistical significance

The significance of differences of DLHP or MHP angles at different stages with or without QVD treatment (Figures 1L and S1H) and of the release after ablation (Figure 2H) was assessed using a t-test, considering embryos as independent from each other. The null hypothesis was that the true difference between the means of these group is zero.

The significance of differences in nucleus displacement, deformation, and fragmentation (Figures 3J, 3L, and 3M), in the angle of apical deformation (Figure 4B), in the speed of apical pulling or release (Figure 4C), in the quantification of apoptosis (Figure S1G), in the apico-basal position of nuclei (Figure S3D), and in the relative displacement of nuclei (Figure S3E) was assessed using the Mann-Whitney test. The null hypothesis was that the measurements were samples from the same distribution.

The significance of differences in variance distribution of the orientation of cells neighboring an apoptotic or a control cell (Figures 4E and 4F) was assessed using the Levene test. The null hypothesis was that the measurements were samples from the same variance.

Statistics were performed in python script (levene test), Prism and excel. Significance is denoted as follows according to the p value: ****$p<0.0001$; ***$p<0.001$; **$p<0.01$; *$p<0.05$; NS $p>=0.05$ (not significant).

Box plot were generated with Prism, Polar plots were generated with python.